Selective homonuclear 2D J-resolved spectroscopy

Davy Sinnaeve

This is the submitted version (before peer-review) of:

eMagRes, 2021, Vol 9: 267–282. DOI 10.1002/9780470034590.emrstm1544

The final and edited version can be found at
https://doi.org/10.1002/9780470034590.emrstm1544

Selective homonuclear 2D J-resolved spectroscopy

Davy Sinnaeve[1,2]

[1]Univ. Lille, Inserm, Institut Pasteur de Lille, CHU Lille, U1167 – Labex DISTALZ – RID-AGE – Risk Factors and Molecular Determinants of Aging-Related Diseases, F-59000 Lille, France

[2]CNRS, ERL9002 – Integrative Structural Biology, F-59000 Lille, France

davy.sinnaeve@univ-lille.fr

KEYWORDS

2D J-resolved spectroscopy, selective pulses, pure shift NMR, SERF, G-SERF, PSYCHEDELIC, scalar couplings, residual dipolar couplings, Zangger-Sterk, PSYCHE

ABSTRACT

Selective 2D J-resolved spectroscopy delivers 2D spectra where exclusively homonuclear couplings to a selected spin feature as doublets along the indirect dimension, facilitating their measurement. The original experiment, SERF, uses frequency-selective pulses in order to manipulate the evolution of particular couplings. This basic principle has been improved and expanded upon in many follow-up experiments over the years. Experiments using the Zangger-Sterk or PSYCHE pulse sequence elements have resulted in variants called G-SERF and PSYCHEDELIC respectively, and allow observation of a wider spectral bandwidth and decoupling of spins with close chemical shifts. Also strategies to achieve high-resolution full absorption mode line shapes have been proposed. Finally, homonuclear decoupling methods have been introduced to suppress couplings to non-selected spins in the spectrum and thus avoid spectral overlap. Rather than providing a historic and comprehensive overview of the many different variations of SERF, this article presents the selective 2D J-resolved spectroscopy as a modular experiment, where these various features can be introduced to fit a particular situation. Advantages and drawbacks of each variation is discussed.

1. INTRODUCTION

Couplings between protons represent a wealth of structural information, as they provide insight to molecular constitution, configuration and conformation. However, accurately measuring their values from simple 1D spectra can be very complicated. If one proton is involved in many couplings, it leads to intricate multiplets where the individual splittings may be difficult or impossible to resolve. This worsens when different multiplets overlap in the spectrum. For this reason, much effort has gone into developing experiments where the readout provides just one selected coupling at a time, *i.e.*, a simple doublet, while maximally avoiding any interference from other spectral responses. Seminal work was performed by Stefan Berger in 1995, reporting the SERF (Selective ReFocusing) 2D experiment.[1] Derived from 2D J-resolved spectroscopy (*see* emrstm0579.pub2),[2] it uses doubly selective pulses to pick a pair of protons so that only the coupling between these two protons is observed as a doublet along the indirect dimension. The basic principle of using frequency-selective pulses to tailor which ^{1}H-^{1}H couplings appear in the spectrum laid the foundation for many follow-up experiments that further improved and facilitated coupling measurement for increasingly challenging cases. These innovations mostly occurred in parallel with advances in 2D J-spectroscopy in general[3] and with the emergence of pure shift NMR spectroscopy[4-5] (*see* emrstm1362). The latter is not surprising, given that pure shift methods likewise edit the manifestation of homonuclear couplings in the spectrum. Besides frequency-selective pulses, as used in SERF, several other pulse sequence elements that refocus coupling evolution (so-called Active Spin Refocusing (ASR) elements) have been proposed in the context of pure shift methods. These ASR elements can equally be applied in SERF, resulting in variants such as G-SERF[6] and PSYCHEDELIC.[7]

Rather than providing a historical perspective or a comprehensive summary of known selective 2DJ experiments — of which excellent reviews already exist,[8-9] most notably the

one by Stefan Berger[8] — the purpose of this article is to present a 'technical manual' of all the pulse sequence components that make up modern variants of the SERF experiment. This didactic overview make readers familiar with all basic underlying principles, allowing them to make an informed choice on which particular SERF variant best suits their needs or how to design their own experiments.

2. MAIN TEXT

2.1 The basic selective 2DJ experiment

A selective 2DJ experiment is any 2D homonuclear J-resolved experiment that uses frequency-selective pulses so that the spectrum only features a limited number of homonuclear couplings in the indirect (F_1) dimension. The basic principles of how chemical shift and homonuclear coupling evolutions can be manipulated will first be introduced. Only protons that are coupled under the weak coupling regime will be considered, allowing the use of product operator formalism (*see* emrstm1310). Under the condition of strong coupling, more complicated secondary order effects occur whose description fall outside the scope of this article.[10-13] We first consider the basic spin echo, *i.e.*, the original homonuclear 2DJ sequence (Figure 1A).[2]. Consider a spin I (the "observed" spin) with two coupling partners S (the "selected" spin) and X (the "passive" spin). To represent the senses of chemical shift and coupling evolutions, the use of the shift product operator basis is the most convenient. Assume that, after 90° pulse excitation, spin I has coherence order of +1 immediately after the excitation pulse, and thus a negative sense of chemical shift evolution. The spin-states of X and S are denoted as p and q respectively, which each can be either α or β. The inverted spin-states of X and S are then denoted as $\overline{p}$ and $\overline{q}$, so that, for instance, if $p = \alpha$ then $\overline{p} = \beta$ and vice versa. Chemical shift and coupling evolutions during the 2DJ sequence can then be derived:

$$
\begin{aligned}
&\mathrm{I}^{+}\mathrm{X}^{p}\mathrm{S}^{q} \xrightarrow{(t_1/2)(\Omega_\mathrm{I}\mathrm{I}_z+2\pi J_\mathrm{IX}\mathrm{I}_z\mathrm{X}_z+2\pi J_\mathrm{IS}\mathrm{I}_z\mathrm{S}_z)} \mathrm{I}^{+}\mathrm{S}^{p}\mathrm{X}^{q}e^{-i\pi(mJ_\mathrm{IX}+nJ_\mathrm{IS})t_1/2}e^{-i\Omega_\mathrm{I}t_1/2} \\
&\xrightarrow{180°(\mathrm{I}_x+\mathrm{X}_x+\mathrm{S}_x)} \mathrm{I}^{-}\mathrm{X}^{\overline{p}}\mathrm{S}^{\overline{q}}e^{-i\pi(mJ_\mathrm{IX}+nJ_\mathrm{IS})t_1/2}e^{-i\Omega_\mathrm{I}t_1/2} \\
&\xrightarrow{(t_1/2)(\Omega_\mathrm{I}\mathrm{I}_z+2\pi J_\mathrm{IX}\mathrm{I}_z\mathrm{X}_z+2\pi J_\mathrm{IS}\mathrm{I}_z\mathrm{S}_z)} \mathrm{I}^{-}\mathrm{X}^{\overline{p}}\mathrm{S}^{\overline{q}}e^{-i\pi(mJ_\mathrm{IX}+nJ_\mathrm{IS})t_1} \\
&\xrightarrow{t_2(\Omega_\mathrm{I}\mathrm{I}_z+2\pi J_\mathrm{IX}\mathrm{I}_z\mathrm{X}_z+2\pi J_\mathrm{IS}\mathrm{I}_z\mathrm{S}_z)} \mathrm{I}^{-}\mathrm{X}^{\overline{p}}\mathrm{S}^{\overline{q}}e^{-i\pi(mJ_\mathrm{IX}+nJ_\mathrm{IS})t_1}e^{-i\pi(mJ_\mathrm{IX}+nJ_\mathrm{IS})t_2}e^{i\Omega_\mathrm{I}t_2}
\end{aligned}
\qquad (1)
$$

with m and n equal to +1 or –1 depending on whether p and q are equal to α or β respectively. Figure 1A introduces a diagram representing the sense of chemical shift evolution (equivalent to a coherence transfer pathway (CTP) diagram, except for its opposite sign) and the evolution of the J_{IX} and J_{IX} couplings throughout the sequence. Such diagram provides the same information as the product operator analysis, and is very useful to quickly visualize and evaluate which type of information has built up or has been refocused during the sequence. The hard 180° pulse reverses the sense of chemical shift evolution of I, so that it is refocused over t_1 and sampled during t_2. Because the hard 180° pulse also inverts the spin-states of S and X, the sense of J_{IX} and J_{IS} coupling evolutions are not reversed and thus build up during t_1, with the same sense of evolution as during t_2. After double Fourier transform the resulting 2D spectrum (Figure 1A) shows four lines, representing all possible combinations of spin-states of S and X. The chemical shift information is found only along F_2, and since the couplings were equally encoded during both t_1 and t_2, the individual peaks within the multiplet are dispersed parallel to a –45° axis between F_1 and F_2. Because chemical shift and coupling information are encoded along different angles in the 2D spectrum, these two types of spectral information are essentially separated. This facilitates multiplet analysis relative to the 1D spectrum where multiplets can overlap. It is standard procedure to tilt the 2DJ spectra by 45° to align the multiplets fully along F_1, thus creating a (J,δ)-representation.[14] In practice, the 2D data is sheared, which distorts slightly the line shapes. <Figure 1 near here>

Whereas in full 2DJ spectrum all homonuclear couplings evolve during t_1, a selective 2DJ spectrum aims to sample only the evolution of a selected coupling (or couplings) during t_1. It is clear that this requires an inversion of the J_{IX} coupling evolution, which can be done using a so-called Active Spin Refocusing (ASR) element. This is an element that has the property of reversing the sense of chemical shift evolution of the observed spin I without inverting the spin-states of its coupling partners X and S. Several such ASR elements have been proposed, as will be discussed in the following section. Figure 1B shows a 2DJ sequence where the hard 180° pulse is replaced by an ASR element. The product operator analysis of this sequence is:

$$\begin{aligned} &\mathrm{I}^{+}\mathrm{X}^{p}\mathrm{S}^{q} \xrightarrow{(t_1/2)(\Omega_\mathrm{I}\mathrm{I}_z+2\pi J_{\mathrm{IX}}\mathrm{I}_z\mathrm{X}_z+2\pi J_{\mathrm{IS}}\mathrm{I}_z\mathrm{S}_z)} \mathrm{I}^{+}\mathrm{X}^{p}\mathrm{S}^{q}e^{-i\pi(mJ_{\mathrm{IX}}+nJ_{\mathrm{IS}})t_1/2}e^{-i\Omega_\mathrm{I}t_1/2} \\ &\xrightarrow{ASR} \mathrm{I}^{-}\mathrm{X}^{p}\mathrm{S}^{q}e^{-i\pi(mJ_{\mathrm{IX}}+nJ_{\mathrm{IS}})t_1/2}e^{-i\Omega_\mathrm{I}t_1/2} \xrightarrow{(t_1/2)(\Omega_\mathrm{I}\mathrm{I}_z+2\pi J_{\mathrm{IX}}\mathrm{I}_z\mathrm{X}_z+2\pi J_{\mathrm{IS}}\mathrm{I}_z\mathrm{S}_z)} \mathrm{I}^{-}\mathrm{X}^{p}\mathrm{S}^{q} \qquad (2) \\ &\xrightarrow{t_2(\Omega_\mathrm{I}\mathrm{I}_z+2\pi J_{\mathrm{IX}}\mathrm{I}_z\mathrm{X}_z+2\pi J_{\mathrm{IS}}\mathrm{I}_z\mathrm{S}_z)} \mathrm{I}^{-}\mathrm{X}^{p}\mathrm{S}^{q}e^{i\pi(mJ_{\mathrm{IX}}+nJ_{\mathrm{IS}})t_2}e^{i\Omega_\mathrm{I}t_2} \end{aligned}$$

As the ASR element does not invert the spin-states of X and S, coupling evolution is reversed and thus also refocused over t_1. This can be observed visually from the diagram in Figure 1B. As no information is sampled along t_1, all lines of the multiplet are now found parallel to F_2 in the resulting 2D spectrum, meaning no separation of chemical shift and coupling information. In order to selectively reintroduce the coupling evolution to spin S, a soft 180° inversion pulse is introduced that only affects spin S (Figure 1C). This frequency-selective pulse will be referred to from now on as the Ω_S-selective pulse. Since the duration of such a soft pulse is usually long, chemical shift and coupling evolutions during the pulse cannot be neglected, and may also be complicated by Bloch-Siegert effects.[15] For this reason, a complementary Ω_S-selective pulse is performed at the start of the sequence, so that phase evolutions taking place during these pulses cancel out thanks to the refocusing properties of the ASR element. The product operator analysis of this sequence is (neglecting for simplicity chemical shift and coupling evolution taking place during both frequency-selective 180° pulses, as they cancel out):

$$
\begin{aligned}
&\mathrm{I}^{+}\mathrm{X}^{p}\mathrm{S}^{q} \xrightarrow{180°(\mathrm{S}_x)} \mathrm{I}^{+}\mathrm{X}^{p}\mathrm{S}^{\bar{q}} \\
&\xrightarrow{(t_1/2)(\Omega_\mathrm{I}\mathrm{I}_z+2\pi J_\mathrm{IX}\mathrm{I}_z\mathrm{X}_z+2\pi J_\mathrm{IS}\mathrm{I}_z\mathrm{S}_z)} \mathrm{I}^{+}\mathrm{X}^{p}\mathrm{S}^{\bar{q}} e^{-i\pi(mJ_\mathrm{IX}-nJ_\mathrm{IS})t_1/2} e^{-i\Omega_\mathrm{I}t_1/2} \\
&\xrightarrow{ASR} \mathrm{I}^{-}\mathrm{X}^{p}\mathrm{S}^{\bar{q}} e^{-i\pi(mJ_\mathrm{IX}-nJ_\mathrm{IS})t_1/2} e^{-i\Omega_\mathrm{I}t_1/2} \xrightarrow{180°(\mathrm{S}_x)} \mathrm{I}^{-}\mathrm{X}^{p}\mathrm{S}^{q} e^{-i\pi(mJ_\mathrm{IX}-nJ_\mathrm{IS})t_1/2} e^{-i\Omega_\mathrm{I}t_1/2} \qquad (3) \\
&\xrightarrow{(t_1/2)(\Omega_\mathrm{I}\mathrm{I}_z+2\pi J_\mathrm{IX}\mathrm{I}_z\mathrm{X}_z+2\pi J_\mathrm{IS}\mathrm{I}_z\mathrm{S}_z)} \mathrm{I}^{-}\mathrm{X}^{p}\mathrm{S}^{q} e^{i\pi nJ_\mathrm{IS}t_1} \\
&\xrightarrow{t_2(\Omega_\mathrm{I}\mathrm{I}_z+2\pi J_\mathrm{IX}\mathrm{I}_z\mathrm{X}_z+2\pi J_\mathrm{IS}\mathrm{I}_z\mathrm{S}_z)} \mathrm{I}^{-}\mathrm{X}^{p}\mathrm{S}^{q} e^{i\pi nJ_\mathrm{IS}t_1} e^{i\pi(mJ_\mathrm{IX}+nJ_\mathrm{IS})t_2} e^{i\Omega_\mathrm{I}t_2}
\end{aligned}
$$

Exclusively the coupling evolution with spin S is now encoded in t_1. As shown in Figure 1C, this leads to a 2DJ spectrum where the splittings due to the coupling with X remain parallel to F_2, but those from the coupling with S are again parallel to a –45° axis. The latter coupling is thus effectively separated from both chemical shift and the passive coupling information. When a projection is made onto the F_1 axis, the J_IS coupling is effectively found as a simple doublet response, greatly facilitating its extraction by avoiding all complications arising from the crowding of lines within a full multiplet. Just as the full 2DJ spectrum, the selective 2DJ spectrum can be tilted by 45°, in this case delivering a (J_IS, $\delta + J_\mathrm{IX}$)-representation. Because the sense of J_IS coupling evolution during t_1 and t_2 is identical, just as in the classical 2DJ experiment, the experiment of Figure 1C is referred to as Normal type (N-type). Figure 1D shows an alternative sequence where the positions of the $t_1/2$ delays and the Ω_S-selective pulses are swapped. The result from product operator analysis (or inspection of the diagram in Figure 1G) is in this case:

$$\mathrm{I}^{-}\mathrm{X}^{p}\mathrm{S}^{q} e^{-i\pi nJ_\mathrm{IS}t_1} e^{i\pi(mJ_\mathrm{IX}+nJ_\mathrm{IS})t_2} e^{i\Omega_\mathrm{I}t_2} \qquad (4)$$

The sense of J_IS coupling evolution during t_1 is opposite relative to t_2, and this experiment is thus named the Reversed type (R-type). The J_IS couplings are dispersed parallel to a 45° axis rather than a –45° axis in the resulting 2D spectrum.

Although the selective 2DJ experiment singled out a single coupling, a number of important issues remain at this point. First, all experiments in Figure 1 will deliver 2D spectra with

peaks possessing the phasetwist line shape,[11] which is highly unfavorable for accurate coupling measurement. Approaches to fix this issue will be discussed in the section "***Full absorption mode line shapes***". Second, the passive couplings remain along F_2, meaning that a pure chemical shift dimension is not obtained and multiplets may still overlap. The suppression of passive couplings in F_2 will be dealt with in the section "***Homonuclear decoupling: pure shift spectroscopy***". Before addressing these issues, the question of how active spin refocusing is achieved will first be addressed in the following section.

2.2 Active spin refocusing

Different ASR elements are available (Figure 2), and its choice will define the class of the selective 2DJ experiment. Each ASR element comes with its own advantages and limitations, and the best choice mainly depends on the problem at hand. The most straightforward ASR element is simply another frequency-selective 180° pulse, this time set to the resonance frequency of spin I and thus here referred to as a Ω_I-selective pulse. All signals that fall outside the bandwidth of the Ω_I-selective pulse are edited out of the spectrum by phase cycling or by pulsed magnetic field gradients (*see* emrstm1344 *and* emrstm0164). Such selective 2DJ spectra are named SERF (SElective REfocusing) experiments, and is equivalent to the original experiment proposed by Fäcke and Berger (which used a single (Ω_I,Ω_S)-biselective 180° pulse, Figure 3).[1] The active spin refocusing is here thus achieved solely by exploiting the difference in resonance frequency between spin I and its coupling partners X and S. As will become clear when discussing the other ASR elements, the main advantage of SERF is that it generally suffers the lowest sensitivity penalty, as the only magnetization losses come from pulse imperfections and relaxation during the soft pulse. The main limitation of SERF is that it only works well when the spectral band excited by the Ω_I-selective pulse only contains resonances of spins that are not coupled to each other. If this is not the case, active spin refocusing breaks down and more complicated multiplets will be

found in F_1. As shown in the original work by Fäcke and Berger (Figure 3),[1] the SERF experiment is thus mostly used to measure couplings one by one by setting both the Ω_I- and Ω_S-selective pulses to a single resonance each. Occasionally, it is feasible to simultaneously select more than one spin (I_1, I_2,..) with the Ω_I-selective pulse that are coupling partners of the selected proton S without violating the aforementioned limitation (*i.e.*, I_1, I_2,.. are not coupled to each other), but in general one cannot expect to observe all coupling partners of spin S in one SERF spectrum. This makes SERF to most restrictive class of selective 2DJ experiments. <Figure 2 near here> <Figure 3 near here>

A second class of selective 2DJ experiments is G-SERF (Gradient SElective REfocsing), first proposed by Giraud *et al.*[6] It makes use of the Zangger-Sterk ASR element,[16] which essentially is a Ω_I-selective 180° pulse extended with a magnetic field gradient applied simultaneously (*see* emrstm1528). The magnetic field gradient disperses the resonance frequencies of all spins spatially across the sample in a linear fashion. Typically *z*-gradients are applied, though *xy*-gradients have been used[17]. In this way, a different spectral region is affected by the Ω_I-selective pulse at each spatial coordinate in the sample (Figure 4A). To ensure that at a certain spatial coordinate a spin is not excited along with a coupling partner, the bandwidth of the Ω_I-selective pulse must be chosen less than the minimal difference in resonance frequency found between any pair of coupled observed spins. Active spin refocusing is then achieved for each spin in one experiment at different spatial coordinates in the sample. The strength of the magnetic field gradient determines the spectral range that is dispersed over the active volume of the sample, and thus the total spectral band that will be observed in the G-SERF spectrum. The advantage of this approach is thus that active spin refocusing can be achieved for a broad range of chemical shifts, making it possible to simultaneously observe all couplings involving the selected spin S. However, the sensitivity is much reduced compared to the SERF experiment, as the detected nuclei are limited to a slice

of the sample. The thickness of the slice is proportional to the ratio between the bandwidth of the Ω_I-selective pulse with the total spectral bandwidth to be observed (controlled by the magnetic field gradient strength). The strength of the G-SERF experiment is thus its tunability, as it allows trading broadband character for sensitivity. Its weakness is that the sensitivity penalty can be very severe when active spin refocusing must be achieved when coupled spins have small chemical shift differences. This also means that an optimal setup of Zangger-Sterk element greatly relies on having the assignment of the spectrum available. Furthermore, the long duration of the magnetic field gradient may lead to significant diffusional and convectional signal attenuation[18] (*see* emrstm1388). A positive effect of detecting only a reduced volume is that line broadening due to magnetic field inhomogeneity is much reduced, meaning sharper lines along F_2, especially when very inhomogeneous samples are studied. Although generally applicable to any situation, G-SERF will be the most effective when only a limited chemical shift range is of interest or the spins that have to be decoupled have large chemical shift differences. <Figure 4 near here>

The third ASR element that has been used for selective 2DJ experiments is the PSYCHE element (Pure Shift Yielded by CHirp Excitation), first introduced by Foroozandeh *et al*.[19] This class of selective 2DJ experiments are referred to as PSYCHEDELIC (Pure Shift Yielded by CHirp Excitation to DELiver Individual Couplings).[7] Rather than exploiting frequency differences, PSYCHE uses low flip angle RF-pulses to achieve the inversion of the observed spins with retention of the spin-states of its coupling partners. This principle bears a strong analogy to the *z*-COSY and anti-*z*-COSY experiments.[20-21] To understand PSYCHE, it is very instructive to first analyze the effect of two pulses with low flip angle β., as in such *z*-COSY experiments. The effect of the first RF-pulse with flip angle β is:

$$\mathrm{I}^{+}\mathrm{X}^{p}\mathrm{S}^{q} \xrightarrow{\beta(\mathrm{I}_x+\mathrm{X}_x+\mathrm{S}_x)} \left(\mathrm{I}^{\alpha}\mathrm{X}^{p}\mathrm{S}^{q} - \mathrm{I}^{\beta}\mathrm{X}^{p}\mathrm{S}^{q}\right)(i/2)\sin(\beta)\cos^{4}(\beta/2) \qquad (5)$$

$$+\left(\mathrm{I}^{\alpha}\mathrm{X}^{\bar{p}}\mathrm{S}^{q}-\mathrm{I}^{\beta}\mathrm{X}^{\bar{p}}\mathrm{S}^{q}\right)(i/2)\sin(\beta)\cos^{2}(\beta/2)\sin^{2}(\beta/2)$$

$$+\left(\mathrm{I}^{\alpha}\mathrm{X}^{p}\mathrm{S}^{\bar{q}}-\mathrm{I}^{\beta}\mathrm{X}^{p}\mathrm{S}^{\bar{q}}\right)(i/2)\sin(\beta)\cos^{2}(\beta/2)\sin^{2}(\beta/2)$$

$$+\left(\mathrm{I}^{\alpha}\mathrm{X}^{\bar{p}}\mathrm{S}^{\bar{q}}-\mathrm{I}^{\beta}\mathrm{X}^{\bar{p}}\mathrm{S}^{\bar{q}}\right)(i/2)\sin(\beta)\sin^{4}(\beta/2)$$

$$+\text{zero-, single-, and multiple-quantum terms}$$

The zero-, single-, and multiple-quantum coherences are then eliminated using a zero-quantum filter.[22] Thus, only considering further the population terms, the effect of the next β-pulse is:

$$\xrightarrow{\beta(\mathrm{I}_x+\mathrm{X}_x+\mathrm{S}_x)}\quad \mathrm{I}^{-}\mathrm{X}^{p}\mathrm{S}^{q}(1/8)\sin^{2}(\beta)\,(1+\cos^{2}(\beta))^{2}$$

$$+\mathrm{I}^{-}\mathrm{X}^{\bar{p}}\mathrm{S}^{q}(1/8)\sin^{4}(\beta)\,(1+\cos^{2}(\beta))$$

$$+\mathrm{I}^{-}\mathrm{X}^{p}\mathrm{S}^{\bar{q}}(1/8)\sin^{4}(\beta)\,(1+\cos^{2}(\beta))$$

$$+\mathrm{I}^{-}\mathrm{X}^{\bar{p}}\mathrm{S}^{\bar{q}}(1/8)\sin^{6}(\beta)$$

$$+\left(m\mathrm{I}^{\alpha}\mathrm{X}^{-}\mathrm{S}^{q}-m\mathrm{I}^{\beta}\mathrm{X}^{-}\mathrm{S}^{q}+n\mathrm{I}^{\alpha}\mathrm{X}^{p}\mathrm{S}^{-}-n\mathrm{I}^{\beta}\mathrm{X}^{p}\mathrm{S}^{-}\right)\times(1/8)\sin^{2}(\beta)\cos^{2}(\beta)\,(1+\cos^{2}(\beta)) \tag{6}$$

$$+\left(m\mathrm{I}^{\alpha}\mathrm{X}^{-}\mathrm{S}^{\bar{q}}-m\mathrm{I}^{\beta}\mathrm{X}^{-}\mathrm{S}^{\bar{q}}+n\mathrm{I}^{\alpha}\mathrm{X}^{\bar{p}}\mathrm{S}^{-}-n\mathrm{I}^{\beta}\mathrm{X}^{\bar{p}}\mathrm{S}^{-}\right)\times(1/8)\sin^{4}(\beta)\cos^{2}(\beta)$$

$$+\text{ other terms with coherence order different from }-1$$

The terms with coherence orders different from –1 are easily suppressed using phase cycling or pulsed field gradients. The remaining terms can be divided into three categories. Firstly, the $\mathrm{I}^{-}\mathrm{X}^{p}\mathrm{S}^{q}$ term, where the spin-states of the coupling partners have not changed, is what leads to active spin refocusing and produces the wanted responses in the selective 2DJ spectrum. Secondly, the terms where the –1 coherence order ends up on spin I and the spin-state of spins X and/or S are inverted will not lead to a refocusing of all coupling evolutions in the selective 2DJ sequence, and thus result in additional responses in the spectrum known as 'recoupling artefacts'.[23] Thirdly, terms are generated where the –1 coherence order ends up on spins S or X. These deliver responses in the 2DJ spectrum that may be called 'z-COSY

artefacts', as it is these that produce the cross-peaks the *z*-COSY experiment.[20] However, in selective 2DJ experiments they are not desired, and will have similar intensity to the wanted responses. The latter two categories of unwanted responses must thus be attenuated, while retaining the first category. To deal with the *z*-COSY artefacts, the β-pulses of the PSYCHE element are given as frequency-swept (chirp) pulses applied simultaneously with a magnetic field gradient (Figure 2C).[19, 23] This setup essentially adds a spatially dependent phase to the magnetization of spin I in the first half of the PSYCHE element by an amount that is determined by the chemical shift of spin I. In the second half of PSYCHE, another spatially dependent phase term is added with opposite sense by an amount determined by the chemical shift of the spin where the –1 coherence order ended up. The resulting net phase terms of the product operators of the first two categories in equation 6 will thus be zero, but the operators of the third category experience a net phase term proportional to the difference in chemical shift between spin I and X or S, leading to an attenuation of the *z*-COSY artefacts in a very similar way as in zero-quantum filters.[22] Longer frequency-swept pulses will lead to overall better suppression of these artefacts, but this is traded for sensitivity, since this will also result in higher relaxation, diffusion and convection losses during the PSYCHE element.[23] Next, in order to reduce the recoupling artefacts relative to the wanted responses, the flip angle β is kept sufficiently low. Equation 6 shows that the intensity of the wanted responses is proportional to $\sin^2(\beta)\,(1+\cos^2(\beta))^2$, while the most intense recoupling artefacts are proportional to $\sin^4(\beta)\,(1+\cos^2(\beta))$. The artefact to signal ratio is thus $\sin^2(\beta)/(1+\cos^2(\beta))$. For $\beta = 20°$, the intensity of the recoupling artefacts is thus only about 6% relative to the wanted responses. The idea is thus to choose a compromise value of the flip angle, so that it is high enough to have sufficient sensitivity for the desired responses, but low enough so that the recoupling artefacts are sufficiently weak and ideally fall below the noise level. Typically, flip angles between 10° and 25° are chosen, resulting in a

sensitivity penalty relative to the 1D ^{1}H spectrum of about an order of magnitude.[19] Note that the intensities of both the wanted and artefact responses were derived here explicitly for a spin with two coupling partners. For *N* coupling partners of spin I, the intensities of the desired responses and the most intense recoupling artefacts will be respectively $2^{-(N+1)}\sin^2(\beta)\,(1+\cos^2(\beta))^N$ and $2^{-(N+1)}\sin^4(\beta)\,(1+\cos^2(\beta))^{N-1}$. In principle, the sensitivity penalty is thus slightly different for each multiplet, especially for higher flip angles. Finally, in practice, the frequency-swept pulses in PSYCHE are amplitude-modulated (saltire pulses) rather than phase-modulated, implying frequency is swept in both directions simultaneously, providing better sensitivity without reducing the signal to recoupling artefact ratio compared to unidirectional sweeps.[19, 23-24]

Overall, the PSYCHE element is thus all about trading sensitivity for spectral purity, *i.e.*, the absence of unwanted responses. This contrasts with the Zangger-Sterk element, where in principle perfect spectral purity can be achieved, but a compromise must be made between sensitivity and observed spectral bandwidth. PSYCHE is thus a good general use ASR element, as it imposes nearly no restrictions on the observed bandwidth of the spectrum, delivers good sensitivity with a spectral purity that is usually satisfactory, and works well even when coupled spins have close chemical shifts. Also its setup is independent from chemical shifts, so that spectral assignment is not needed beforehand. However, the Zangger-Sterk element will typically outperform PSYCHE both in terms of sensitivity and spectral purity in cases where only a limited region of the spectrum is of interest and the coupled protons are *a priori* known to have sufficiently large chemical shift differences.

Finally, other ASR elements have been described, such as BIRD[25] and time reversal.[26] These will not be discussed here, as they have not yet found direct application in selective 2DJ experiments (although BIRD has been used in a related setup to measure geminal ^{1}H-^{1}H couplings[27]).

2.3 Full absorption mode line shapes

Just as in classical 2DJ spectroscopy, the peaks in selective 2DJ spectra using the experimental setup as described in Figure 1 will feature the so-called phasetwist line shape (Figure 5A).[11] This is very damaging to both spectral resolution and the accuracy of coupling measurement, and ways to avoid this line shape warrant considerable attention. To analyze its origin and remedies, a two-spin IS spin system will be considered here for simplicity. First, the explicit expressions of the one-dimensional absorption (*A*) and dispersion (*D*) mode line shapes are introduced. This is done along F_1 for peaks at coordinates $\pi n J_{\mathrm{IS}}$ and $-\pi n J_{\mathrm{IS}}$, and along F_2 at coordinate $\Omega_{\mathrm{I}} + \pi n J_{\mathrm{IS}}$. <Figure 5 near here>

$$A_1^{\pm} = \mathrm{Re}\left\{\mathrm{FT}\left\{e^{\pm i\pi n J_{\mathrm{IS}} t_1} e^{-t_1/T_2}\right\}\right\} = \frac{T_2}{1 + (\omega_1 \mp \pi n J_{\mathrm{IS}})^2 T_2^2} \tag{7}$$

$$D_1^{\pm} = \mathrm{Im}\left\{\mathrm{FT}\left\{e^{\pm i\pi n J_{\mathrm{IS}} t_1} e^{-t_1/T_2}\right\}\right\} = \frac{-(\omega_1 \mp \pi n J_{\mathrm{IS}}) T_2^2}{1 + (\omega_1 \mp \pi n J_{\mathrm{IS}})^2 T_2^2} \tag{8}$$

$$A_2 = \mathrm{Re}\left\{\mathrm{FT}\left\{e^{i(\Omega_{\mathrm{I}} + \pi n J_{\mathrm{IS}}) t_2} e^{-t_2/T_2}\right\}\right\} = \frac{T_2}{1 + (\omega_2 - \Omega_{\mathrm{I}} - \pi n J_{\mathrm{IS}})^2 T_2^2} \tag{9}$$

$$D_2 = \mathrm{Im}\left\{\mathrm{FT}\left\{e^{i(\Omega_{\mathrm{I}} + \pi n J_{\mathrm{IS}}) t_2} e^{-t_2/T_2}\right\}\right\} = \frac{-(\omega_2 - \Omega_{\mathrm{I}} - \pi n J_{\mathrm{IS}}) T_2^2}{1 + (\omega_2 - \Omega_{\mathrm{I}} - \pi n J_{\mathrm{IS}})^2 T_2^2} \tag{10}$$

It is seen that the absorption mode line shape is symmetric and the dispersion mode line shape is anti-symmetric relative to the middle of the F_1-axis:

$$A_1^+[-\omega_1] = A_1^-[\omega_1] \tag{11}$$

$$D_1^+[-\omega_1] = -D_1^-[\omega_1] \tag{12}$$

To understand the origin of the phasetwist line shape, consider the time-domain signal coming from the $\mathrm{I}^-\mathrm{S}^q$ term detected at the end of the N-type selective 2DJ experiment (Figure 1C and equation 3, without the J_{IX} coupling and including the effects of T_2 relaxation):

$$s_N(t_1, t_2) = e^{i\pi n J_{\mathrm{IS}} t_1} e^{-t_1/T_2} e^{i(\Omega_{\mathrm{I}} + \pi n J_{\mathrm{IS}}) t_2} e^{-t_2/T_2} \tag{13}$$

Fourier transform with respect to t_1 and t_2 provides the peak shape of one half of the doublet:

$$s_N(\omega_1, \omega_2) = (A_1^+ + iD_1^+)(A_2 + iD_2) = (A_1^+A_2 - D_1^+D_2) + i(A_1^+D_2 + D_1^+A_2) \quad (14)$$

The real part of this shape is the phasetwist line shape, and it is an inseparable mixture of the absorption and dispersion mode line shapes (Figure 5A).[11] The presence of the dispersion component gives the phasetwist line shape a much wider profile than the full absorption mode line shape (Figure 5B) with both negative and positive tails. Not only does this impair spectral resolution, partial overlap between two peaks will influence the positions of their maxima in a complex way, thus spoiling coupling measurement accuracy. The dispersion components can be purged by time-domain weighting and magnitude mode processing, but at a severe cost in sensitivity.[28] Avoiding the phasetwist line shape altogether is greatly preferred. Fortunately, it is possible to modify the selective 2DJ experiment so that full absorption mode line shapes are delivered.

In the context of selective 2DJ spectroscopy, two approaches have been used. The first is the *z*-filter (Figure 6).[29] First applied to SERF (the resulting experiment called SERFph),[30-31] the *z*-filter is appended to the sequence and consists out of two hard 90° pulses sandwiching a zero-quantum filtration step, such as an adiabatic frequency-swept 180° pulse applied during a weak magnetic field gradient.[22] Assuming perfect 90° pulse rotations, a *z*-filter purges all homonuclear antiphase coherences, retaining only in-phase magnetization. This is illustrated for an N-type selective 2DJ sequence, placing the *z*-filter between the t_1 incremented delays and the direct acquisition period (Figure 6A). We consider in this case explicitly both possible spin-states of S during t_1. The terms obtained just before the *z*-filter can then be split into an in-phase and an anti-phase term, where the latter is then purged by the *z*-filter:

$$\begin{aligned} &\mathrm{I}^-\mathrm{S}^\alpha e^{i\pi J_{\mathrm{IS}} t_1} e^{-t_1/T_2} + \mathrm{I}^-\mathrm{S}^\beta e^{-i\pi J_{\mathrm{IS}} t_1} e^{-t_1/T_2} \\ &= \underbrace{\mathrm{I}^-\left(\mathrm{S}^\alpha + \mathrm{S}^\beta\right)}_{\text{in-phase}} \cos(\pi J_{\mathrm{IS}} t_1)\, e^{-t_1/T_2} + i\,\underbrace{\mathrm{I}^-\left(\mathrm{S}^\alpha - \mathrm{S}^\beta\right)}_{\text{anti-phase}} \sin(\pi J_{\mathrm{IS}} t_1)\, e^{-t_1/T_2} \\ &\xrightarrow{z\text{-filter}} \mathrm{I}^-\left(\mathrm{S}^\alpha + \mathrm{S}^\beta\right) \cos(\pi J_{\mathrm{IS}} t_1)\, e^{-t_1/T_2} \end{aligned} \quad (15)$$

Besides the –1 → –1 coherence order pathway, the *z*-filter equally permits the +1 → –1 pathway, yielding an identical result:

$$\begin{aligned} &\mathrm{I}^{+}\mathrm{S}^{\alpha} e^{-i\pi J_{\mathrm{IS}} t_1} e^{-t_1/T_2} + \mathrm{I}^{+}\mathrm{S}^{\beta} e^{i\pi J_{\mathrm{IS}} t_1} e^{-t_1/T_2} \\ &\xrightarrow{z-\mathrm{filter}} \mathrm{I}^{-}\left(\mathrm{S}^{\alpha} + \mathrm{S}^{\beta}\right) \cos(\pi J_{\mathrm{IS}} t_1)\, e^{-t_1/T_2} \end{aligned} \tag{16}$$

The total detected signal coming from either the $\mathrm{I}^{-}\mathrm{S}^{\alpha}$ and $\mathrm{I}^{-}\mathrm{S}^{\beta}$ term during the t_2 acquisition period is thus the sum of both these pathways:

$$s_{N,zf}(t_1, t_2) = 2\cos(\pi J_{\mathrm{IS}} t_1)\, e^{-t_1/T_2} e^{i(\Omega_{\mathrm{I}} + \pi n J_{\mathrm{IS}}) t_2} e^{-t_2/T_2} \tag{17}$$

Which, after Fourier transform with respect to t_2 becomes:

$$s_{N,zf}(t_1, \omega_2) = 2\cos(\pi J_{\mathrm{IS}} t_1)\, e^{-1/T_2 t_1} (A_2 + iD_2) \tag{18}$$

At this point, only the real part of the data is considered, and subsequent Fourier transform with respect to t_1 provides the final 2D spectrum:

$$\begin{aligned} s_{N,zf}(\omega_1, \omega_2) &= \mathrm{FT}\left\{\mathrm{Re}\left\{s_{N,zf}(t_1, \omega_2)\right\}\right\} \\ &= (A_1^{+} A_2 + A_1^{-} A_2) + i(D_1^{+} A_2 + D_1^{-} A_2) \end{aligned} \tag{19}$$

The real part of the *z*-filtered selective 2DJ spectrum now features full absorption mode line shapes. However, for each response in F_2, two peaks are now found along F_1, at πJ_{IS} and $-\pi J_{\mathrm{IS}}$, and so a doubling of the total number of peaks in the 2D spectrum compared to the non-*z*-filtered experiment (Figure 1C). A *z*-filter essentially destroys the bijective relation between the spin-states of S during t_1 and those during t_2. The practical consequence of the resulting 'rectangular' 2D pattern is that the J_{IS} splitting can no longer be removed from the F_2 axis by 45° tilting. <Figure 6 near here>

A second approach to achieve full absorption mode line shape was introduced by Pell and Keeler for full 2DJ spectroscopy, and so generally referred to as the Pell-Keeler method.[32] It involves recording two 2DJ datasets that differ only in their sense of coupling evolution during t_1. The original Pell-Keeler method for full 2DJ spectra required the introduction of an

ASR element to manipulate the sense of coupling evolution of all couplings simultaneously. However, for selective 2DJ experiments, only the evolution of couplings to the selected spin S must be controlled, since the passive couplings are anyway refocused during t_1, an insight that was first described for the PSYCHEDELIC experiment.[7] As was already shown in Figures 1C and D, this is easily achieved by reshuffling the relative order of the t_1 incrementation delays and the Ω_S-selective pulses, resulting in either an N- or an R-type selective 2DJ experiment. The way by which this leads to full absorption mode line shapes is very similar to the echo/anti-echo processing method used in 2D NMR.[33] Consider the signals obtained from both the N- and R-type spectra, including the effects of relaxation:

$$\begin{aligned} s_N(t_1, t_2) &= e^{i\pi n J_{IS} t_1} e^{-t_1/T_2} e^{i(\Omega_I + \pi n J_{IS}) t_2} e^{-t_2/T_2} \\ s_R(t_1, t_2) &= e^{-i\pi n J_{IS} t_1} e^{-t_1/T_2} e^{i(\Omega_I + \pi n J_{IS}) t_2} e^{-t_2/T_2} \end{aligned} \tag{20}$$

Taking for each the Fourier transform with respect to t_2:

$$\begin{aligned} s_N(t_1, \omega_2) &= e^{i\pi n J_{IS} t_1} e^{-t_1/T_2} (A_2 + iD_2) \\ s_R(t_1, \omega_2) &= e^{-i\pi n J_{IS} t_1} e^{-t_1/T_2} (A_2 + iD_2) \end{aligned} \tag{21}$$

These datasets are then recombined into new ones, after taking the complex conjugate of the R-type dataset:

$$\begin{aligned} s^+(t_1, \omega_2) &= s_N(t_1, \omega_2) + s_R(t_1, \omega_2)^* = 2e^{i\pi n J_{IS} t_1} e^{-t_1/T_2} A_2 \\ s^-(t_1, \omega_2) &= -i(s_N(t_1, \omega_2) - s_R(t_1, \omega_2)^*) = 2e^{i\pi n J_{IS} t_1} e^{-t_1/T_2} D_2 \end{aligned} \tag{22}$$

Finally, after Fourier transform with respect to t_1:

$$\begin{aligned} s^+(\omega_1, \omega_2) &= 2A_1^+ A_2 + 2iD_1^+ A_2 \\ s^-(\omega_1, \omega_2) &= 2A_1^+ D_2 + 2iD_1^+ D_2 \end{aligned} \tag{23}$$

The real part of $s^+(\omega_1, \omega_2)$ has full absorption mode line shape. Although in practice this method is usually applied on time domain data in the way just described, it is very instructive to consider it from the perspective of frequency domain data. Taking the Fourier transform

with respect to both t_1 and t_2 of the N- and R-type signals, as shown in Figure 7A and 7B, both spectra display phasetwist line shapes:

$$s_N(\omega_1, \omega_2) = (A_1^+ A_2 - D_1^+ D_2) + i(A_1^+ D_2 + D_1^+ A_2)$$
$$s_R(\omega_1, \omega_2) = (A_1^- A_2 - D_1^- D_2) + i(A_1^- D_2 + D_1^- A_2) \quad (24)$$

Taking the complex conjugate of the R-type t_1 time domain data (equation 21) is equivalent to reversing the F_1-axis in the frequency domain, as shown in Figure 7C, positioning the 2D peaks at the same position as in the N-type spectrum. Considering relations 11 and 12;, this becomes:

$$s_R(-\omega_1, \omega_2) = (A_1^+ A_2 + D_1^+ D_2) + i(A_1^+ D_2 - D_1^+ A_2) \quad (25)$$

From this it is clear that $s_N(\omega_1, \omega_2) + s_R(-\omega_1, \omega_2) = s^+(\omega_1, \omega_2)$. Figure 7D illustrates that indeed the dispersion components of the phasetwist line shape of the N-type and F_1-reversed R-type spectra cancel out, but the absorptive parts add up. <Figure 7 near here>

Both *z*-filter and Pell-Keeler strategies have specific benefits. The *z*-filter is more prone to artefact signals that result from unwanted coherence transfer pathways that seep through via pulse imperfections,[34] while the long delay needed for zero-quantum suppression leads to relaxation losses. In contrast, the Pell-Keeler method introduces no additional RF-pulses or delays relative to the parent selective 2DJ experiment, thus generally providing the cleanest and most sensitive result. Also, the Pell-keeler method retains the property of dispersing the selected couplings along a –45° axis, thus reducing the likelihood of multiplet overlap in crowded spectra compared to *z*-filtered spectra. The main advantage of the *z*-filtered approach is that it is faster, allowing full absorption mode line shapes using just one transient per t_1 increment, while the Pell-Keeler method requires recording both N- and R-type datasets. Furthermore, a *z*-filter purges any homonuclear anti-phase magnetization, thus also in cases where the ASR element turns out not fully effective. For instance, under conditions of weak molecular alignment, residual dipolar couplings (RDCs) are present (*see* emrstm1240 *and*

emrstm1194), and in contrast to scalar couplings these manifest themselves in the spectrum between equivalent protons. Typical cases are geminal ^{1}H-^{1}H RDCs between chemical shift degenerate protons within methyl or methylene groups. Bandselective and Zangger-Sterk elements fail to discriminate between chemical shift degenerate protons, meaning splittings from the dipolar couplings between them also appear along F_1 together with the couplings chosen via the selective pulses. (Incidentally, PSYCHE can decouple such protons, but additional artefact peaks appear.[35]) Since for such couplings the sense of evolution during t_1 is not controlled by the selective pulses, the Pell-Keeler method breaks down and phasetwist line shapes are obtained,[35] but the *z*-filter will still work.[36] Similarly, a *z*-filter also provides full absorption mode line shapes for geminal ^{1}H-^{1}H scalar coupling evolution that is not refocused by the BIRD element.[27]

2.4 Homonuclear decoupling: pure shift spectroscopy

On the one hand, the purpose of full 2D J-resolved spectroscopy is the separation of multiplets from chemical shift information, thus avoiding multiplets from clashing. On the other hand, selective 2DJ spectroscopy aims to single out an individual coupling to facilitate its extraction, but all passive couplings remain along F_2. Figure 8B shows an example of a 2D PSYCHEDELIC experiment that uses the Pell-Keeler method for absorption mode line shapes, applied on 17β-estradiol.[7] Selection of proton H9 develops individual couplings along F_1 for protons H8, H11α and H11β. However, because H8 and H11β have close chemical shifts, the multiplets formed by the passive couplings along F_2 overlap, complicating the extraction of the individual couplings along F_1. It would be very useful if all passive couplings would be suppressed in F_2, so that multiplet overlap is entirely avoided. Figure 8E shows a PSYCHEDELIC spectrum where exactly this is achieved using pure shift methods, and only couplings to H9 are found along F_1 and F_2. It is clear that the spectrum drastically simplifies, and measurement of all couplings to H9 becomes straightforward. Pure shift

experiments[4-5] are closely related to 2D J-resolved spectroscopy, and their combination with selective 2DJ methods is a logical one since they are based on the same principle of active spin refocusing as already discussed above. <Figure 8 near here>

Consider an ASR element in combination with a hard 180° pulse, as in the sequence of Figure 9A. As seen from the phase evolution diagram, the sense of chemical shift evolution taking place before and after these two pulses is identical and thus builds up during t_1, while coupling evolution during t_1 is refocused. By incrementing t_1, an interferogram can be constructed by measuring a single complex time domain point at the end of the second $t_1/2$ period for each increment. By pasting these together, an FID is constructed that contains pure chemical shift information. This method, first proposed by Garbow, Weitekamp and Pines,[25] would take an unreasonable amount of t_1 increments and thus experimental time to obtain a 1D spectrum with useful digital resolution, discouraging its application. Zangger and Sterk were the first to realize that the number of t_1 increments can be drastically reduced by measuring a chunk of time domain data (of duration τ_{ch}) rather than sampling individual data points.[16] This setup was further improved by Morris and coworkers[37-38] as shown in Figure 9B. Homonuclear couplings are refocused in the middle of each chunk, but because couplings evolve at a much slower rate than chemical shifts, we can get away with sampling many time domain points before and after that point. The price to pay is the presence of so-called chunking artefacts in the final pure shift spectrum. This will be illustrated here assuming two spins I and S. By inspecting the chemical shift and coupling evolution diagrams in Figure 9B, it can be seen that in the middle of the chunk chemical shift has evolved over a net period $t_1 + \tau_{ch}/2$, while coupling evolution is perfectly refocused, resulting in the terms:

$$\mathrm{I^-S^\alpha} e^{i\Omega_\mathrm{I}(t_1+\tau_{ch}/2)} + \mathrm{I^-S^\beta} e^{i\Omega_I(t_1+\tau_{ch}/2)} = \left(\mathrm{I^-S^\alpha} + \mathrm{I^-S^\beta}\right) e^{i\Omega_\mathrm{I}(t_1+\tau_{ch}/2)} \qquad (26)$$

With $\mathrm{I^-S^\alpha} + \mathrm{I^-S^\beta}$ representing in-phase magnetization of spin I. At the edges of the chunk, coupling evolution is not perfectly refocused. For instance, at the end of the chunk:

$$\mathrm{I^-S^\alpha} e^{i\Omega_\mathrm{I}(t_1+\tau_{ch})} e^{i\pi J_\mathrm{IS}\tau_{ch}/2} + \mathrm{I^-S^\beta} e^{i\Omega_\mathrm{I}(t_1+\tau_{ch})} e^{i\pi J_\mathrm{IS}\tau_{ch}/2}$$

$$= \left(\mathrm{I^-S^\alpha} + \mathrm{I^-S^\beta}\right) e^{i\Omega_\mathrm{I}(t_1+\tau_{ch})} \cos(\pi J_\mathrm{IS}\,\tau_{ch}/2) \qquad (27)$$

$$- i\left(\mathrm{I^-S^\alpha} - \mathrm{I^-S^\beta}\right) e^{i\Omega_\mathrm{I}(t_1+\tau_{ch})} \sin(\pi J_\mathrm{IS}\,\tau_{ch}/2)$$

With $I^-S^\alpha - I^-S^\beta$ representing anti-phase magnetization of spin I. Only the in-phase component represents detectable signal. The signal intensity at the edges of the chunk are thus attenuated by a factor $\cos(\pi J_\mathrm{IS}\,\tau_{ch}/2)$ relative to what would have been obtained if only chemical shift had evolved. The ideal pure shift FID, as would be obtained by the experiment of Figure 9A, is represented by $e^{i\Omega_\mathrm{I}t_1'}$, with t_1' the time domain of the reconstructed FID. The difference between this ideal pure shift FID and the reconstructed FID obtained by using data chunking of Figure 9B is what represents the chunking artefacts:

$$e^{i\Omega_\mathrm{I}t_1'}(1 - \cos(\pi J_\mathrm{IS}[\{t_1'(\mathrm{mod}\,\tau_{ch})\} - \tau_{ch}/2])) \qquad (28)$$

The Fourier transform of this function is a periodic set of overtone peaks centered around Ω_I that are interspaced by $1/\tau_{ch}$ and harmonically decline in intensity. The intensity of these chunking artefacts relative to the parent pure shift signal is proportional to $1 - \cos(\pi J_\mathrm{IS}\,\tau_{ch}/2)$. Keeping the chunk duration sufficiently short so that $\tau_{ch} \ll 2/\pi J_\mathrm{IS}$ will thus keep these artefacts at acceptable levels. In practice, this is achieved with chunks of 10-20 ms long, typically about two orders of magnitude longer than the dwell time and thus greatly boosting the acquisition speed relative to the experiment of Figure 9A. <Figure 9 near here>

A second strategy to obtain a pure shift FID is shown in Figure 9D, known as real-time acquisition.[39] In this case, the combination of an ASR element and 180° pulse is repeated several times per transient rather than spread over different increments, and data chunks are measured in between the pulses. Coupling evolution is refocused close to (but not exactly at[40]) the middle of the chunk. Just as in the interferogram approach, the data chunks are recombined to yield a pure shift FID. Also, a short ASR echo must be applied as a preparation

step before the start of acquisition so that the ASR element already discards signal before the start of data acquisition, for instance signals falling outside the pulse bandwidth in case of a Ω_I-selective pulse. Compared to interferogram acquisition of data chunks, the obvious advantage of the real-time method is the greatly reduced experimental time, essentially falling back to a single transient. The drawback is that magnetization losses occurring between the chunks, such as from relaxation or pulse imperfections, are additive, resulting in an apparently increased signal decay during the pure shift FID and thus broader resonances compared to the interferogram experiment. Especially for long ASR elements, such as highly selective Ω_I-selective pulses or Zangger-Sterk elements, this can be problematic. Also, the PSYCHE element is incompatible with this approach,[5] since each time it is applied it will independently act as a magnetization filter, as opposed to Ω_I-selective pulse, Zangger-Sterk or BIRD elements.

In the same way as for selective 2DJ experiments, Ω_S-selective pulses can be introduced in pure shift experiments to reinstate couplings to a selected spin. The sequence of Figure 9C shows this for an interferogram setup. Couplings to spin S are refocused at the start of the first chunk ($t_1 = 0$) instead of its middle, and experience a net evolution during t_1. An example of such interferogram experiment is the '1D' version of the PSYCHEDELIC experiment (Figure 8D).[7] Also real-time pure shift experiments can be modified in a similar way by including selective pulses in between the data chunks (Figure 9E). Examples are the real-time SERF experiment, that uses two Ω_S-selective 90° pulses surrounding the hard 180° pulse,[41] and the Quick-SERF experiment that uses a Ω_S-selective 180° pulse.[42] It must be noted that these Ω_S-selective pulses further increase the total delay between data chunks, and thus further broaden resonances in the spectrum compared to the parent real-time pure shift experiment.

Selective reintroduction of couplings in pure shift spectra can be very useful to measure individual couplings, taking just the same experimental time as the parent pure shift

experiment. However, coupling and chemical shift information are mixed in a single dimension, and the resulting doublets may thus again overlap (Figure 8D). In addition, spectral resolution may be limited by magnetic field inhomogeneities, which can be especially cumbersome when measuring small couplings (although approaches exist that can relieve this problem to a certain extent[43]). The most optimal resolution for coupling measurement can thus be achieved by combing the selective 2DJ experiment, where the F_1 dimension does not suffer from magnetic field inhomogeneities, with pure shift resolution along F_2.

2.5 Coupling measurement with maximum resolution: pure shifted selective 2DJ experiments

With all building blocks in hand, the selective 2DJ experiment featuring exclusively couplings to the selected spin can be described. In principle, both types of pure shift acquisition can be combined with either the *z*-filter or Pell-Keeler methods, with an overview given in Figure 10. When an interferogram pure shift acquisition is used, the result is a pseudo-3D experiment, while using the real-time acquisition retains a 2D experimental setup.

<Figure 10 near here>

For *z*-filtered approaches (Figure 10A-B), the pure shift acquisition schemes of Figure 9C or 9E is simply appended to the sequence of Figure 6A. This results in a selective 2DJ experiment where along F_2 only singlets appear, *i.e.*, both couplings to the passive and selected spins are removed (as illustrated in Figure 10F). This thus immediately delivers a (J_{IS},δ)-representation, without having to tilt the spectrum by 45°. Note that in the case of the interferogram experiment of Figure 10A, two ASR elements are needed in total, as chemical shift and pure J_{IS} encoding occur on opposite sides of the *z*-filter element. This has some negative consequences. In SERF and G-SERF experiments, the signal losses from relaxation, pulse imperfections or diffusion during the Ω_I-selective pulses are additive with the number of times they are applied, which may be problematic especially when very selective (and thus

long) pulses are used. Also, it has been shown that non-ideal coherence selection within the ASR element and pulse imperfections within the *z*-filter can conspire to create additional artefact responses in the spectrum.[34] More critically, PSYCHEDELIC experiments are not compatible with this setup, since applying a PSYCHE element twice results in severe signal losses as described above. The real-time pure shift experiment of Figure 10B can function with the same number of ASR elements as its parent real-time pure shift experiment, since the initial magnetization filtration step of the parent experiment is taken care of by the ASR element used for the selective coupling evolution (in practice, T_1 relaxation during the *z*-filter may require also phase cycling). Since PSYCHE is also incompatible with real-time pure shift acquisition, a *z*-filtered PSYCHEDELIC experiment with pure shift acquisition is in general not feasible. Examples of experiments using the strategy of Figure 10A are BSD-SERF[44] and PS-GSERF[45], while an example of the strategy of Figure 10B is push-G-SERF.[46]

Compared to *z*-filtered methods, the Pell-Keeler method turns out very well-suited for designing pure shifted selective 2DJ sequences with an economic use of ASR elements. Indeed, comparison of the Pell-Keeler selective 2DJ sequence (Figure 1C-D) with the interferogram selective pure shift sequence of Figure 9C shows that the former is easily merged with the latter, creating a pseudo-3D experiment (Figure 10C). This setup delivers a pure shifted 2DJ spectrum where the J_{IS} couplings are present in both F_2 and F_1, dispersed along a –45° axis (Figure 10D). After performing a 45° tilt, a (J_{IS},δ)-representation is obtained. Only one ASR element is used, making this setup compatible with PSYCHEDELIC experiments and providing a frugal use of Ω_I-selective pulses in SERF or G-SERF experiments. The original PSYCHEDELIC experiment makes use of this strategy.[7] In theory, also the real-time selective pure shift experimental setup of Figure 9E should be compatible with the Pell-Keeler selective 2DJ experiment, but such experiments have not yet been reported.

Alternatively, it is possible to directly obtain a (J_{IS},δ)-representation using the Pell-Keeler method, and thus a similar spectrum as the *z*-filtered experiments of Figure 10A. This is done simply by moving some of the delays needed for pure shift acquisition (Figure 10E) in such a way that the senses of J_{IS} coupling evolution are opposite during the two $t_2/2$ periods and equal during the two $\tau_{ch}/4$ periods, so that also this coupling is suppressed by the pure shift acquisition scheme. The TSE-PSYCHEDELIC experiment makes use of this experimental setup.[35] In principle, the same can be achieved using the real-time pure shift acquisition of Figure 9D, but also in this case no examples have as of yet been described. Because of the full pure shift resolution in F_2, the resulting N- and R-type spectra now turn out to be equivalent, suggesting that it would suffice to measure just the N-type spectrum and let a copy function as the R-type spectrum. However, there are a good reasons to independently measure the R-type experiment anyway. First, the pure shifted N- and R-type spectra are only perfectly equivalent assuming the weak coupling condition, since strongly coupled spins lead to additional responses in 2DJ spectra that may be scattered in a pattern that is non-symmetrical in F_1.[11-12] A second, more general problem arises at the level of the chunking artefacts. In contrast to the J_{IX} coupling evolution, the J_{IS} couplings experience a net evolution during t_1, meaning the magnetization of spin I will not be purely in-phase in the middle of the chunk relative to the J_{IS} couplings. Applying the same explicit treatment as in the progenitor pure shift experiment (equation 26-28), the magnetization of spin I in the middle of the data chunk for the N- and R-type sequences is:

$$\begin{aligned}&\left(\mathrm{I}^{-}\mathrm{S}^{\alpha}e^{i\lambda\pi J_{\mathrm{IS}}t_1}+\mathrm{I}^{-}\mathrm{S}^{\beta}e^{-i\lambda\pi J_{\mathrm{IS}}t_1}\right)e^{i\Omega_{\mathrm{I}}(t_2+\tau_{ch}/2)}\\&\qquad=\left(\mathrm{I}^{-}\mathrm{S}^{\alpha}+\mathrm{I}^{-}\mathrm{S}^{\beta}\right)\cos(\pi J_{\mathrm{IS}}t_1)\,e^{i\Omega_{\mathrm{I}}(t_2+\tau_{ch}/2)}\\&\qquad+i\lambda\left(\mathrm{I}^{-}\mathrm{S}^{\alpha}-\mathrm{I}^{-}\mathrm{S}^{\beta}\right)\sin(\pi J_{\mathrm{IS}}t_1)\,e^{i\Omega_{\mathrm{I}}(t_2+\tau_{ch}/2)}\end{aligned}\qquad(29)$$

with $\lambda = +1$ for the N-type and $\lambda = -1$ for the R-type experiment. A t_1-dependent mixture of in-phase and anti-phase magnetization is thus obtained. The coefficient of the in-phase term

represents the detectable signal, with the $\cos(\pi J_{\mathrm{IS}} t_1)$ term indicating that an in-phase doublet along F_1 will be obtained after double Fourier transform. At the end of the data chunk, the coupling to spin S will have evolved into:

$$\begin{aligned}\left(\mathrm{I}^{-}\mathrm{S}^{\alpha} e^{i\pi J_{\mathrm{IS}}(\lambda t_1+\tau_{ch}/2)} + \mathrm{I}^{-}\mathrm{S}^{\beta} e^{-i\pi J_{\mathrm{IS}}(\lambda t_1+\tau_{ch}/2)}\right) e^{i\Omega_{\mathrm{I}}(t_2+\tau_{ch})} \\ = \left(\mathrm{I}^{-}\mathrm{S}^{\alpha} + \mathrm{I}^{-}\mathrm{S}^{\beta}\right)(\cos(\pi J_{\mathrm{IS}} t_1)\cos(\pi J_{\mathrm{IS}}\tau_{ch}) \\ - \lambda \sin(\pi J_{\mathrm{IS}} t_1)\sin(\pi J_{\mathrm{IS}}\tau_{ch})) e^{i\Omega_{\mathrm{I}}(t_2+\tau_{ch})} \\ + i\left(\mathrm{I}^{-}\mathrm{S}^{\alpha} - \mathrm{I}^{-}\mathrm{S}^{\beta}\right)(\lambda \sin(\pi J_{\mathrm{IS}} t_1)\cos(\pi J_{\mathrm{IS}}\tau_{ch}) \\ - \cos(\pi J_{\mathrm{IS}} t_1)\sin(\pi J_{\mathrm{IS}}\tau_{ch})) e^{i\Omega_{\mathrm{I}}(t_2+\tau_{ch})}\end{aligned} \quad (30)$$

Clearly, the amount of in-phase magnetization found at the edges of the chunk relative to the middle is different from what was found for the progenitor pure shift experiment (equation 27). When the interferogram would have been constructed measuring individual data points rather than using data chunks, an ideal pure shift FID would be obtained, represented by $\cos(\pi J_{\mathrm{IS}} t_1)\, e^{i\Omega_{\mathrm{I}} t_2'}$, with t_2' the time domain of the reconstructed FID. Similar to equation 28, the difference between this ideal pure shift FID and the reconstructed FID obtained by using chunks is the contribution leading to the chunking artefacts:

$$\begin{aligned}&\cos(\pi J_{\mathrm{IS}} t_1)\, e^{i\Omega_{\mathrm{I}} t_2'}(1 - \cos(\pi J_{\mathrm{IS}}[\{t_2'(\mathrm{mod}\,\tau_{ch})\} - \tau_{ch}/2])) \\ &-\lambda \sin(\pi J_{\mathrm{IS}} t_1)\, e^{i\Omega_{\mathrm{I}} t_2'} \sin(\pi J_{\mathrm{IS}}[\{t_2'(\mathrm{mod}\,\tau_{ch})\} - \tau_{ch}/2])\end{aligned} \quad (31)$$

The first part in this expression starting with the factor $\cos(\pi J_{\mathrm{IS}} t_1)$ represents chunking artefacts that behave in the same way as in the progenitor pure shift spectrum (see equation 28), with intensities proportional to $1 - \cos(\pi J_{\mathrm{IS}}\, \tau_{ch}/2)$ relative to the parent signal, and will appear along F_1 as in-phase doublets. This part of the chunking artefacts is identical in the N- and the R-type experiments. The second part starting with the factor $\lambda \sin(\pi J_{\mathrm{IS}} t_1)$ represents the additional contribution to the chunking artefacts caused by the presence of anti-phase magnetization in the middle of the data chunk. Note that experiments using *z*-filtration avoids this contribution by purging the anti-phase magnetization before pure shift acquisition.[34] The

$\lambda \sin(\pi J_{\mathrm{IS}} t_1)$ term implies that this part of the chunking artefact behaves as an anti-phase doublet along F_1 in the final 2DJ spectrum, and has an opposite sign in the R-type experiment relative to the N-type experiment. At the level of the chunking artefacts, the N- and R-type experiments are thus not equivalent, meaning full absorption mode line shapes of these artefacts can only be achieved by independently measuring both types of spectra. Importantly, the intensities of the anti-phase part of the chunking artefacts relative to the parent pure shift signal are proportional to $\sin(\pi J_{\mathrm{IS}}\, \tau_{ch}/2)$. To keep chunking artefacts small, τ_{ch} must be kept sufficiently short relative to πJ_{IS}. Thus assuming $\pi J_{\mathrm{IS}} \tau_{ch}/2 \ll 1$, the relative intensity of the chunking artefacts that are in-phase along F_1 approximates to $\pi^2 J_{\mathrm{IS}}^2\, \tau_{ch}^2/8$, while for the additional anti-phase contribution this is $\pi J_{\mathrm{IS}}\, \tau_{ch}/2$. The intensity of the anti-phase contribution to the chunking artefacts thus increases faster with τ_{ch} than is the case for the in-phase contribution, and thus imposes shorter chunk lengths than what would have been sufficient for *z*-filtered experiments or the Pell-Keeler experiment of Figure 10C. Rather than shortening τ_{ch} in these experiments, they can be removed in a simple way.[35, 47] The anti-phase character along F_1 implies that this contribution is cancelled by summing the spectrum with its F_1-reverse, while responses in-phase along F_1 are left intact by this operation. However, this only works when all responses have absorption mode line shapes, as these do not invert sign upon F_1-reversal (see equation 11). When peaks possess phasetwist line shapes, whose dispersion mode component invert sign upon F_1-reversal (see equation 12), the anti-phase contribution of the chunking artefacts will not be fully suppressed. The Pell-Keeler method is thus central for minimizing chunking artefact intensities.[35, 47] In practice, this operation can be achieved by taking the sum of $s_N(t_1, \omega_2')$ and $s_R(t_1, \omega_2')$ datasets and zeroing the imaginary part prior to Fourier transform along t_1.[47]

In summary, a variety of different approaches are available to obtain pure shifted selective 2DJ experiments. The Pell-Keeler method combined with interferogram acquisition allows for

any ASR element, including PSYCHE, while its economical use of RF-pulses leads to clean and sensitive spectra.[47] Methods using a *z*-filter retain their advantage of obtaining full absorption mode line shapes in half the amount of transients relative to the Pell-Keeler method.

In most cases, immediate delivery of a (J_{IS},δ)-representation is preferred in order to avoid line shape distortions resulting from 45° tilting. This is the case for *z*-filtered experiments or the Pell-Keeler experiment of Figure 10E. However, *z*-filters, as well as the procedure for suppressing anti-phase chunking artefacts in the experiment of Figure 10E, inherently symmetrize the spectrum along F_1. This may be unfavorable in cases where significant secondary order effects are present, since these produce responses that are non-symmetrical along F_1.[11-12] In such cases, the Pell-Keeler experiment of Figure 10C may be preferred.

Finally, it must be mentioned that in practice pulse sequences are sometimes designed in a slightly different way than depicted in the schemes shown in Figure 10 in order to accommodate other advantageous features. The original PSYCHEDELIC experiment[7] combines the Pell-Keeler method and interferogram PSYCHE pure shift acquisition as in Figure 10C, but uses Broadband Inversion Pulses (BIP) instead of regular 180° pulses.[48] These were found so robust against B_1 field inhomogeneity and B_0 offsets that pulsed field gradients or phase cycling may be omitted.[32] However, BIP pulses used as refocusing pulses must always be applied in pairs in order to cancel out phase errors, and the sequence was designed with four such pulses to accommodate this. Another example is push-G-SERF, which combines a *z*-filter with real-time pure shift Zangger-Sterk acquisition.[46] Rather than using hard 90° RF-pulses, this sequence uses Ω_I-selective 90° pulses applied during a magnetic field gradient, similar to the Zangger-Sterk ASR element. This has the advantage of avoiding excitation of spins that would anyway not have been inversed by the Zangger-Sterk element, thus reducing the need to further suppress these signals. Also, since in this way the

selected spins are not affected by the *z*-filter 90° pulses, zero-quantum coherences are not formed and thus need not be suppressed. On the downside, the Ω_I-selective pulses can become quite long when they need to be very selective, and the large number of such pulses in the sequence can result in considerable relaxation and diffusion losses.

2.6. Conclusion

Following the pioneering SERF experiment by Fäcke and Berger,[1] a large variety of selective homonuclear 2D J-resolved experiments have emerged. Several other extensions of SERF, G-SERF or PSYCHEDELIC experiment have not been discussed in this article, including removal of signals from spins not coupled to the selected spin by using a selective TOCSY or COSY step,[49-50] spatial encoding of the Ω_S-selective pulse using echo planar spectroscopic imaging,[51] use of a perfect echo to compensate for some of the constraints of the ASR element,[52] or expansions to heteronuclear coupling constants,[53-54] to name but a few.[8-9] This list is expected to continue expanding. This article offered a detailed outline of the basic principles that most of these experiments — and likely also future experiments — are based upon. At the time of writing, not every conceivable combination of ASR element, strategy to obtain full absorption mode line shape, and pure shift acquisition method has yet been demonstrated. However, all basic building blocks are well understood, and it is fair to say that the selective 2DJ experiment can be considered as modular, and that an informed choice can be made about the optimal combination given a particular purpose. When new or improved approaches for active spin refocusing are devised, it should be straightforward to incorporate them in selective 2DJ experiments.

3. RELATED ARTICLES

emrstm0579.pub2

emrstm1362

emrstm1528

4. REFERENCES

1. T. Fäcke and S. Berger, *J. Magn. Reson. Ser. A,* 1995, **113**, 114-116.
2. W. P. Aue, J. Karhan and R. R. Ernst, *J. Chem. Phys.,* 1976, **64**, 4226-4227.
3. T. Parella, *Magn. Reson. Chem.,* 2018, **56**, 230-250.
4. L. Castañar and T. Parella, *Magn. Reson. Chem.,* 2015, **53**, 399-426.
5. K. Zangger, *Prog. Nucl. Magn. Reson. Spectrosc.,* 2015, **86-87**, 1-20.
6. N. Giraud, L. Beguin, J. Courtieu and D. Merlet, *Angew. Chem. Int. Ed.,* 2010, **49**, 3481-3484.
7. D. Sinnaeve, M. Foroozandeh, M. Nilsson and G. A. Morris, *Angew. Chem. Int. Ed.,* 2016, **55**, 1090-1093.
8. S. Berger, *Prog. Nucl. Magn. Reson. Spectrosc.,* 2018, **108**, 74-114.
9. Y. Q. Lin, Q. Zeng, L. J. Lin, Z. Chen and P. B. Barker, *Prog. Nucl. Magn. Reson. Spectrosc.,* 2018, **109**, 135-159.
10. A. Kumar and R. R. Ernst, *J. Magn. Reson.,* 1976, **24**, 425-447.
11. G. Bodenhausen, R. Freeman, G. A. Morris and D. L. Turner, *J. Magn. Reson.,* 1978, **31**, 75-95.
12. A. Kumar, *J. Magn. Reson.,* 1978, **30**, 227-249.
13. M. J. Thrippleton, R. A. E. Edden and J. Keeler, *J. Magn. Reson.,* 2005, **174**, 97-109.
14. K. Nagayama, P. Bachmann, K. Wuthrich and R. R. Ernst, *J. Magn. Reson.,* 1978, **31**, 133-148.
15. L. Emsley and G. Bodenhausen, *Chem. Phys. Lett.,* 1990, **168**, 297-303.
16. K. Zangger and H. Sterk, *J. Magn. Reson.,* 1997, **124**, 486-489.
17. N. Giraud, D. Pitoux, J. M. Ouvrard and D. Merlet, *Chem. Eur. J.,* 2013, **19∏**, 12221-12224.
18. M. G. Concilio, P. Kiraly and G. A. Morris, *J. Magn. Reson.,* 2019, **301**, 85-93.
19. M. Foroozandeh, R. W. Adams, N. J. Meharry, D. Jeannerat, M. Nilsson and G. A. Morris, *Angew. Chem. Int. Ed.,* 2014, **53**, 6990-6992.
20. H. Oschkinat, A. Pastore, P. Pfändler and G. Bodenhausen, *J. Magn. Reson.,* 1986, **69**, 559-566.
21. A. J. Pell, R. A. E. Edden and J. Keeler, *Magn. Reson. Chem.,* 2007, **45**, 296-316.
22. M. J. Thrippleton and J. Keeler, *Angew. Chem. Int. Ed.,* 2003, **42**, 3938-3941.
23. M. Foroozandeh, G. A. Morris and M. Nilsson, *Chem. Eur. J.,* 2018, **24**, 13988-14000.
24. M. Foroozandeh, R. W. Adams, P. Kiraly, M. Nilsson and G. A. Morris, *Chem. Commun.,* 2015, **51**, 15410-15413.
25. J. R. Garbow, D. P. Weitekamp and A. Pines, *Chem. Phys. Lett.,* 1982, **93**, 504-509.
26. O. W. Sørensen, C. Griesinger and R. R. Ernst, *J. Am. Chem. Soc.,* 1985, **107**, 7778-7779.
27. N. Marco, P. Nolis, R. R. Gil and T. Parella, *J. Magn. Reson.,* 2017, **282**, 18-26.
28. A. Bax, R. Freeman and G. A. Morris, *J. Magn. Reson.,* 1981, **43**, 333-338.
29. O. W. Sørensen, M. Rance and R. R. Ernst, *J. Magn. Reson.,* 1984, **56**, 527-534.
30. L. Beguin, N. Giraud, J. M. Ouvrard, J. Courtieu and D. Merlet, *J. Magn. Reson.,* 2009, **199**, 41-47.
31. L. Beguin, J. Courtieu, L. Ziani and D. Merlet, *Magn. Reson. Chem.,* 2006, **44**, 1096-1101.
32. A. J. Pell and J. Keeler, *J. Magn. Reson.,* 2007, **189**, 293-299.
33. J. Keeler and D. Neuhaus, *J. Magn. Reson.,* 1985, **63**, 454-472.
34. P. Kiraly, M. Foroozandeh, M. Nilsson and G. A. Morris, *Chem. Phys. Lett.,* 2017, **683**, 398-403.

35. D. Sinnaeve, J. Ilgen, M. E. Di Pietro, J. J. Primozic, V. Schmidts, C. M. Thiele and B. Luy, *Angew. Chem. Int. Ed.,* 2020, **59**, 5316-5320.
36. D. Merlet, L. Beguin, J. Courtieu and N. Giraud, *J. Magn. Reson.,* 2011, **209**, 315-322.
37. M. Nilsson and G. A. Morris, *Chem. Commun.,* 2007, 933-935.
38. J. A. Aguilar, S. Faulkner, M. Nilsson and G. A. Morris, *Angew. Chem. Int. Ed.,* 2010, **49**, 3901-3903.
39. N. H. Meyer and K. Zangger, *Angew. Chem. Int. Ed.,* 2013, **52**, 7143-7146.
40. P. Kiraly, M. Nilsson and G. A. Morris, *Magn. Reson. Chem.,* 2018, **56**, 993-1005.
41. N. Gübensak, W. M. F. Fabian and K. Zangger, *Chem. Commun.,* 2014, **50**, 12254-12257.
42. N. Lokesh, S. R. Chaudhari and N. Suryaprakash, *Chem. Commun.,* 2014, **50**, 15597-15600.
43. S. Glanzer and K. Zangger, *J. Am. Chem. Soc.,* 2015, **137**, 5163-5169.
44. J. E. H. Pucheta, D. Pitoux, C. M. Grison, S. Robin, D. Merlet, D. J. Aitken, N. Giraud and J. Farjon, *Chem. Commun.,* 2015, **51**, 7939-7942.
45. J. E. H. Pucheta, D. Prim, J. M. Gillet and J. Farjon, *ChemPhysChem,* 2016, **17**, 1034-1045.
46. D. Pitoux, B. Plainchont, D. Merlet, Z. Y. Hu, D. Bonnaffe, J. Farjon and N. Giraud, *Chem. Eur. J.,* 2015, **21**, 9044-9047.
47. D. Sinnaeve, *Magn. Reson. Chem.,* 2018, **56**, 947-953.
48. M. A. Smith, H. Hu and A. J. Shaka, *J. Magn. Reson.,* 2001, **151**, 269-283.
49. A. Fredi, P. Nolis and T. Parella, *Magn. Reson. Chem.,* 2017, **55**, 525-529.
50. S. K. Mishra, N. Lokesh and N. Suryaprakash, *RSC Adv.,* 2017, **7**, 735-741.
51. Q. Zeng, L. J. Lin, J. Y. Chen, Y. Q. Lin, P. B. Barker and Z. Chen, *J. Magn. Reson.,* 2017, **282**, 27-31.
52. C. Q. Zhan, Q. Zeng, J. Y. Chen, Y. Q. Lin and Z. Chen, *J. Magn. Reson.,* 2019, **308**, 106590.
53. M. E. Di Pietro, C. Aroulanda and D. Merlet, *J. Magn. Reson.,* 2013, **234**, 101-105.
54. D. Sinnaeve, M. Dinclaux, E. Cahoreau, P. Millard, J. C. Portais, F. Letisse and G. Lippens, *Anal. Chem.,* 2018, **90**, 4025-4031.

BIOGRAPHICAL SKETCH

Davy Sinnaeve, b. 1982. M.Sc. in Chemistry, 2005, Ph.D., 2010, Ghent University, Belgium (directed by J.C. Martins). 2010-2012, Doctor assistant, Ghent University. 2012–2018, Postdoctoral researcher of the Research Foundation – Flanders (FWO). Since 2018, Associate Researcher of the National Center of Scientific Research (CNRS) at the University of Lille. Visiting researcher at the University of Strasbourg in 2012 (with Bruno Kieffer), at the University of Manchester in 2014-2015 (with Gareth A. Morris and Mathias Nilsson), and at the Karlsruhe Institute of Technology in 2017 (with Burkhard Luy). Current main research interests: NMR method and pulse sequence development, structural characterization of proline-rich peptides and proteins.

FIGURES

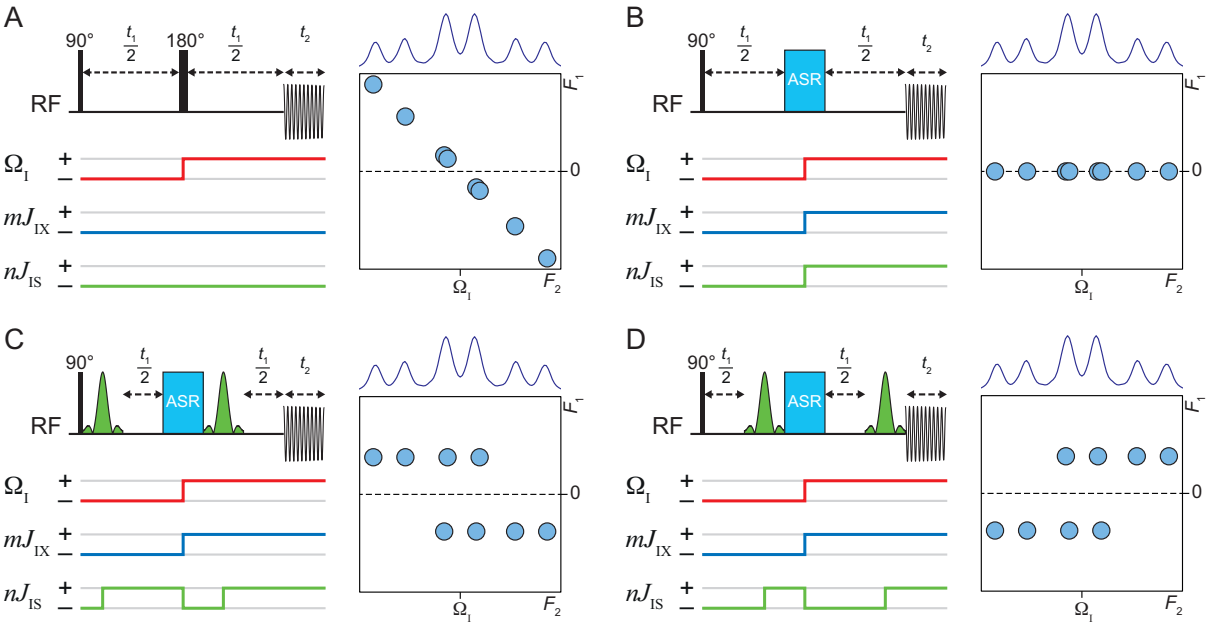

Figure 1

Pulse sequences of (selective) 2D J-resolved experiments, diagrams representing the sense of phase evolutions during the pulse sequences, and schematic representations of the resulting 2D spectra. Narrow and wide black rectangles are respectively 90° and 180° hard RF-pulses. The blue rectangle represents the ASR element. Green shaped pulses are 180° Ω_S-selective RF-pulses. Phase cycles and pulsed field gradients for CTP-selection are omitted for simplicity. The red, blue and green lines indicate the senses of phase evolution due to chemical shift of spin I (Ω_I), J_{IX} couplings and J_{IS} couplings respectively. (A) Original 2DJ experiment; (B) ASR echo experiment; (C) Normal-type selective 2DJ experiment; (D) Reversed-type selective 2DJ experiment.

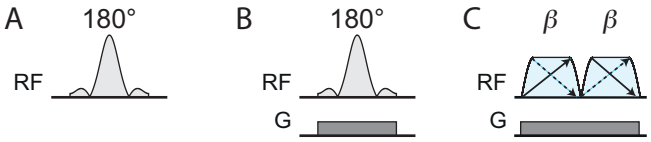

Figure 2

Active spin refocusing elements. (A) Ω_I-selective 180° pulse; (B) Zangger-Sterk element; (C) PSYCHE element. Grey rectangles on line G indicate magnetic field gradients. Trapezoidal pulses with double arrows are low-power frequency-swept chirp pulses of flip angle β, sweeping frequency in both directions simultaneously (saltire pulses).

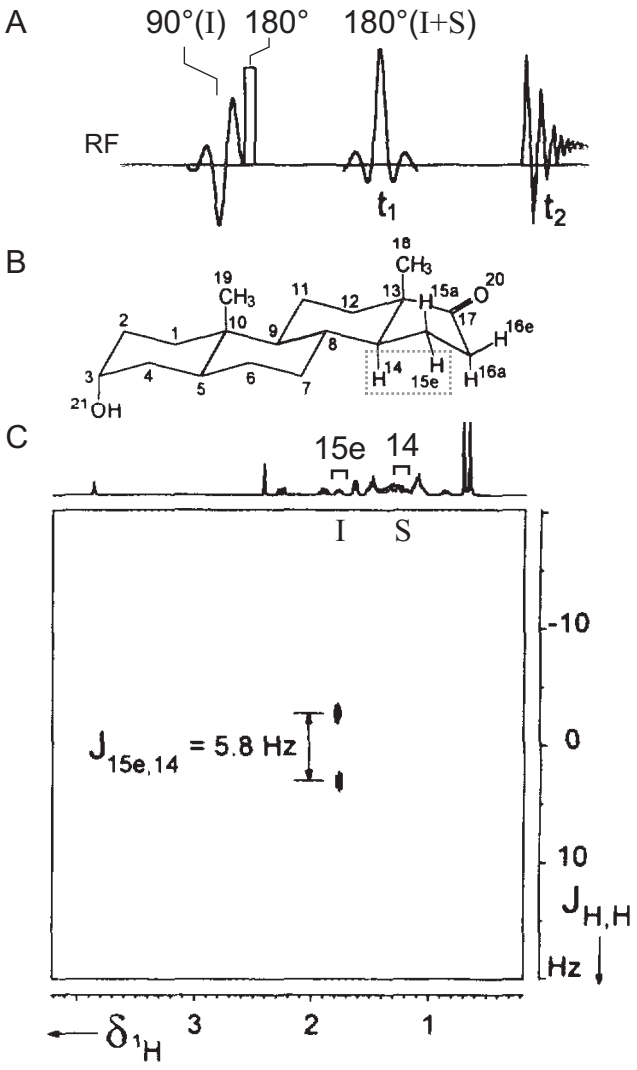

Figure 3

(A) Original SERF experiment, with Ω_I-selective 90° excitation pulse and (Ω_I,Ω_S)-biselective 180° pulse. (B) Molecular structure of androsterone. (C) SERF 2D spectrum, with proton 14 as spin S and proton 15e as spin I, revealing the $J_{15e,14}$ ^{1}H-^{1}H coupling. Reprinted from reference 1, with permission from Elsevier.

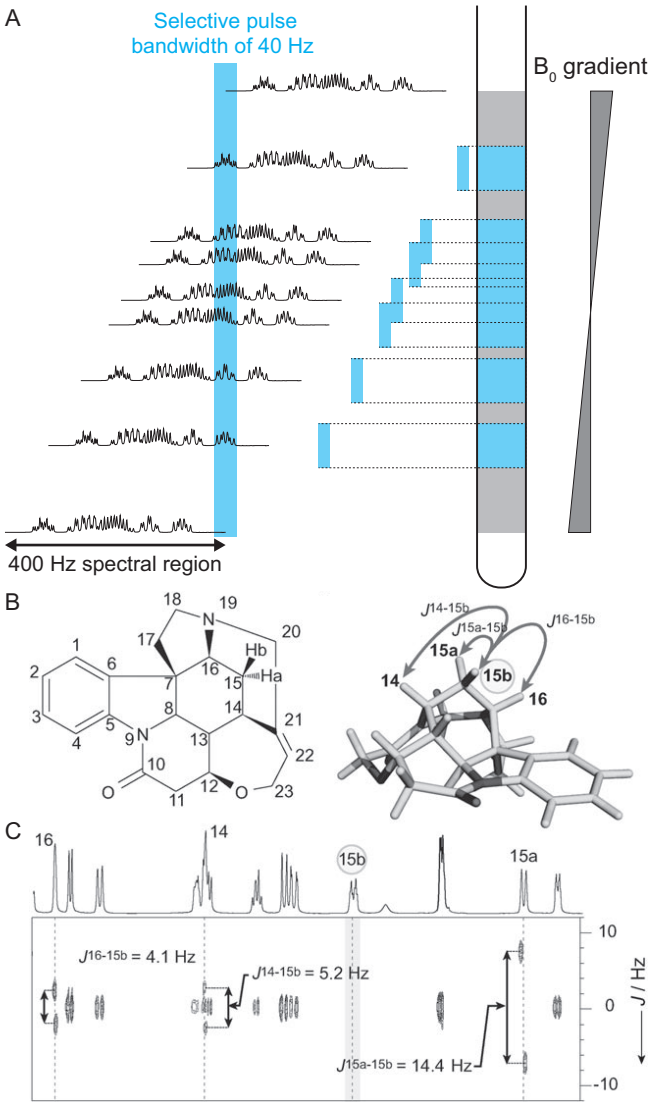

Figure 4

(A) Mechanism of the Zangger-Sterk element. The magnetic field gradient makes the resonance frequencies vary linearly with spatial location, in this example spreading the signals from molecules within the active volume of the sample over a 400 Hz range. The Ω_I-selective 180° pulse excites a narrow bandwidth (40 Hz in this example), so that each resonance is excited only in a particular slice. The thickness of the slice is determined by both the field gradient strength and the bandwidth of the Ω_I-selective pulse. To achieve active spin refocusing, coupling partners must be excited in non-overlapping slices, as determined by the bandwidth of the Ω_I-selective pulse. (B) Planar and 3D structures of strychnine. (C) G-SERF

spectrum, with the Ω_S-selective 180° set to proton 15b. Parts B and C are reproduced from reference 6, with permission from Wiley.

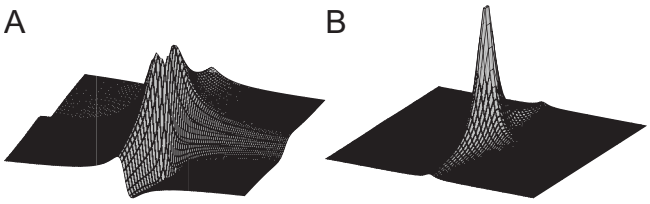

Figure 5

(A) Phasetwist line shape. (B) Full absorption mode line shape.

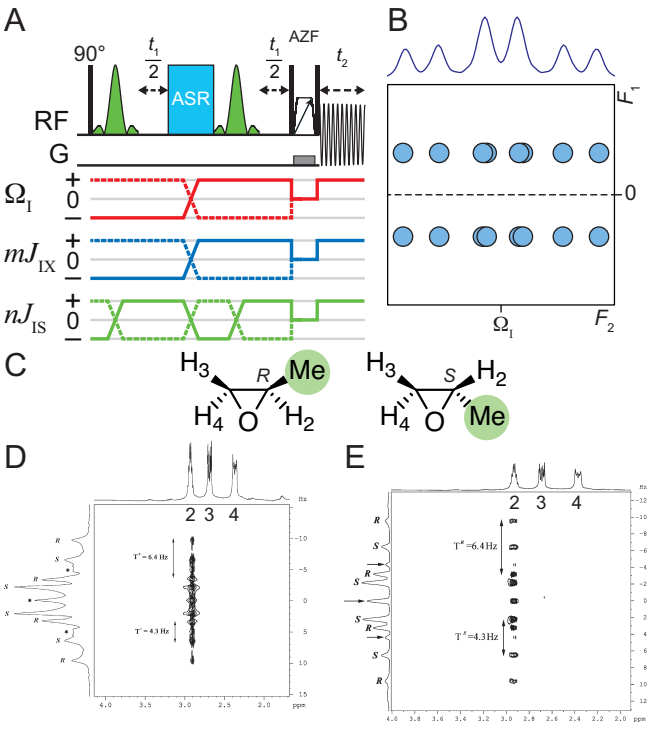

Figure 6

(A) Pulse sequence of a *z*-filtered selective 2DJ experiment. RF pulses and diagrams representing the sense of phase evolutions are as described in Figure 1. The adiabatic *z*-filter (AZF) is indicated, with the trapezoidal pulse with arrow a 180° frequency-swept chirp pulse applied during a magnetic field gradient to suppress zero-quantum artefacts.[22] (B) Schematic representation of the resulting 2DJ spectrum, showing a symmetric pattern along F_1. (C)

Structures of (*R*)- and (*S*)-propyleneoxide. (D) Original SERF spectrum of an enantiomeric mixture of (*R*)- and (*S*)-propylene oxide dissolved in $CDCl_3$ and the chiral alignment medium poly-(γ-benzyl)-L-glutamate, inducing residual dipolar couplings with different values for each enantiomer, allowing enantiomeric excess analysis. The methyl protons are selected by the Ω_S-selective pulse. The phasetwist line shapes obstructs analysis. (E) SERFph experiment on the same sample. The *z*-filter produces absorption mode line shapes, delivering cleaner results. Parts D and E are reproduced from reference 31, with permission from Wiley.

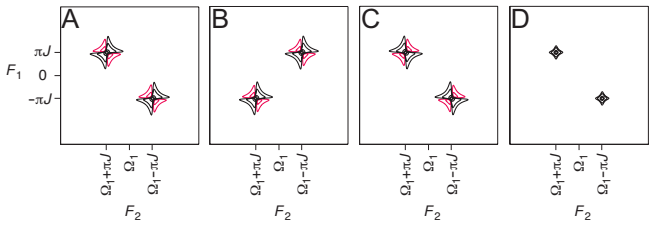

Figure 7

Illustration of the Pell-Keeler method. Positive contours are colored black, negative ones red. Simulated 2DJ spectra of a two-spin system, showing one of both doublets. (A) N-type spectrum. (B) R-type spectrum. Both spectra feature phasetwist line shapes. (C) F_1-reverse of the R-type spectrum. (D) Sum of the N-type and the F_1-reverse of the R-type spectra, providing full absorption mode line shapes. Reprinted from reference 32, with permission from Elsevier.

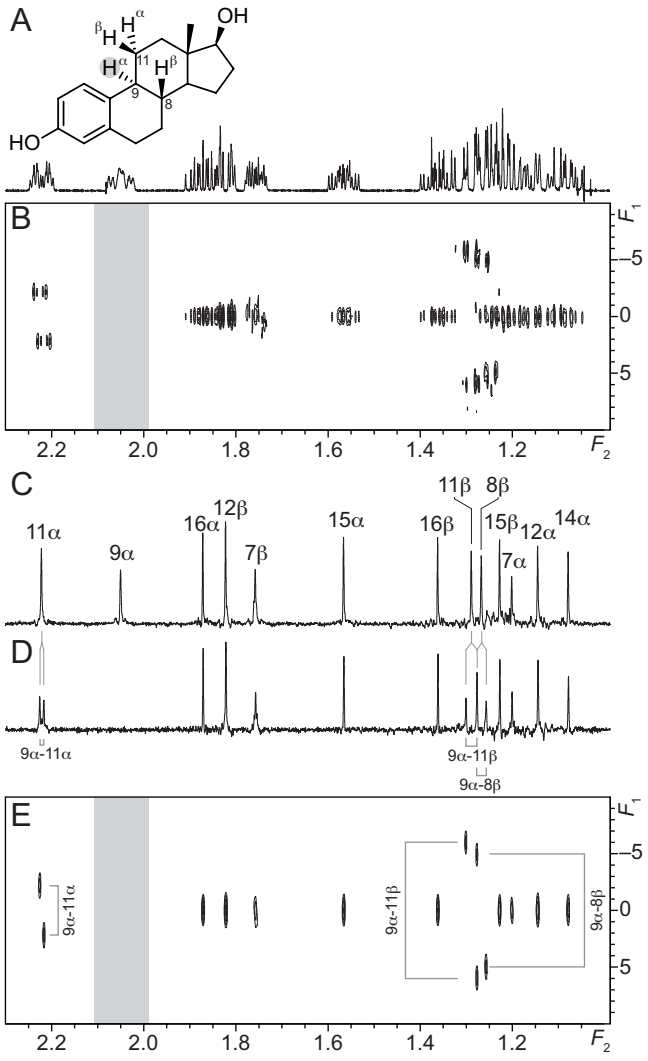

Figure 8

(A) Molecular structure of 17β-estradiol. (B) PSYCHEDELIC spectrum using the Pell-Keeler method, with the Ω_S-selective pulse set to proton 9α (indicated by the grey area), revealing the 9α-8β, 9α-11α and 9α-11β couplings in F_1. The residual 8β and 11β multiplets along F_2 overlap. (C) PSYCHE pure shift spectrum. (D) 1D PSYCHEDELIC spectrum with a Ω_S-selective pulse set to proton 9α. (E) PSYCHEDELIC spectrum using the Pell-Keeler method and interferogram pure shift acquisition, featuring only couplings involving 9α in both F_1 and F_2 dimensions as doublets dispersed parallel to a –45° axis.

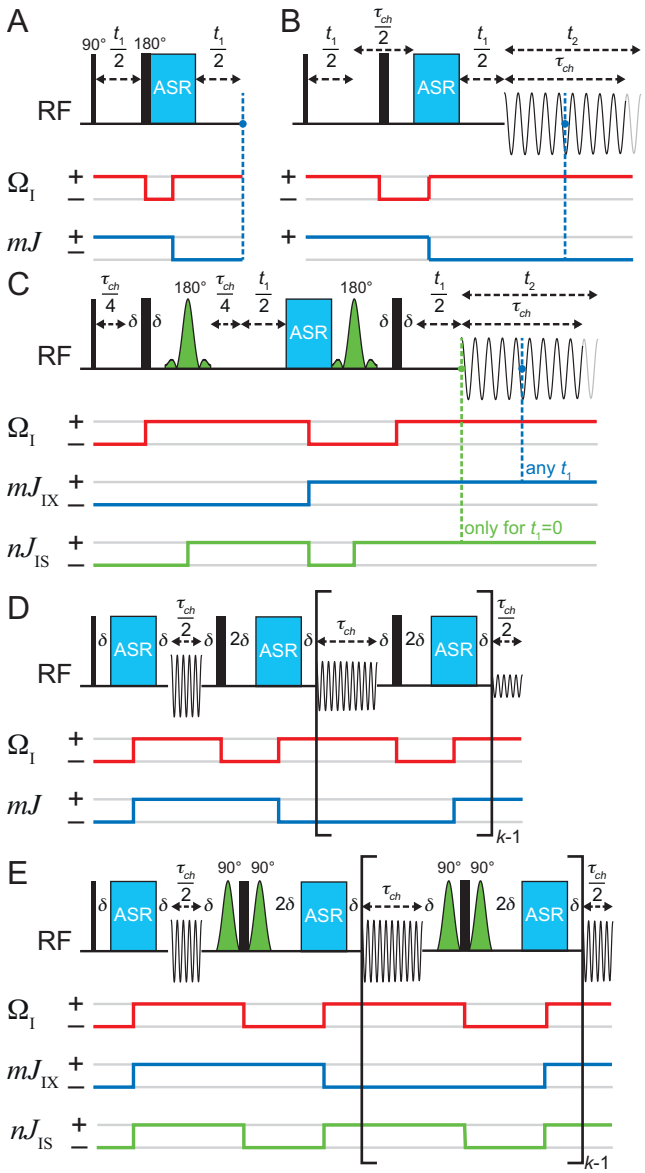

Figure 9

Pulse sequences for pure shift acquisition. (A) Interferogram acquisition strategy with measurement of individual data points.[25] (B) Interferogram acquisition strategy using data chunking.[16, 37-38] (C) Interferogram pure shift experiment with Ω_S-selective pulses. (D) Real-time pure shift acquisition.[39] (E) Real-time pure shift experiment with Ω_S-selective pulses. Black and blue RF pulses are as described in Figure 1. The green shaped pulses which are Ω_S-selective 180° or 90° pulse as indicated. Diagrams representing the sense of phase evolutions are as in Figure 1, except in (A) and (B) where the blue line represents evolution of all

homonuclear couplings. δ is a short delay to accommodate for instance pulsed field gradients. τ_{ch} is the chunk length.

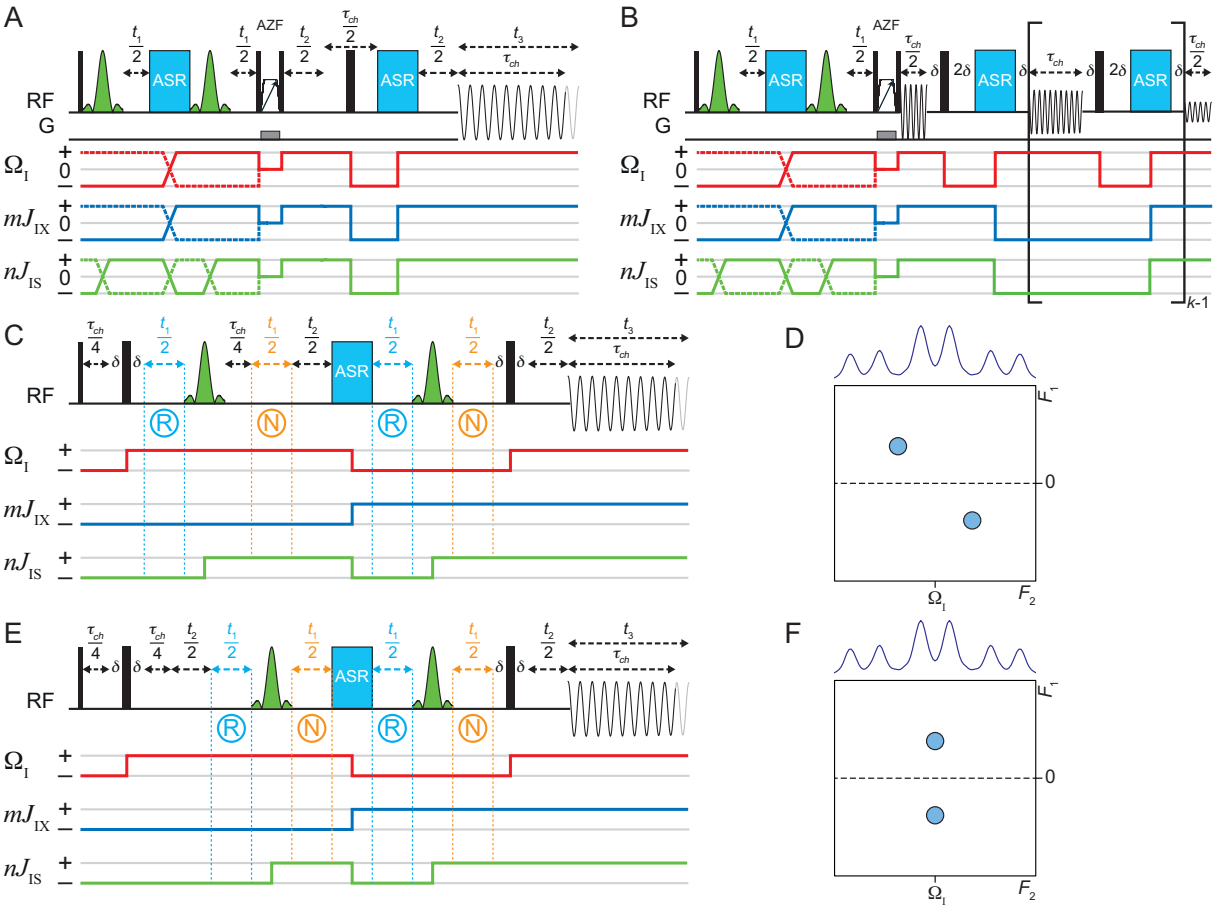

Figure 10

Pure shifted selective 2DJ pulse sequences. (A) *Z*-filtered selective 2DJ experiment with interferogram pure shift acquisition. (B) *Z*-filtered selective 2DJ experiment with real-time pure shift acquisition. (C) Pell-Keeler selective 2DJ experiment with interferogram pure shift acquisition, with the positions of the t_1-delays for the N- and R-type spectra indicated. This experiment delivers 2DJ spectra with couplings dispersed parallel to –45° axis as shown in (D). (E) Pell-Keeler selective 2DJ experiment with interferogram pure shift acquisition, delivering spectra with couplings parallel to F_1 as shown in (F). RF-pulses, delays and diagrams are as described in Figures 1, 6 and 9.